The internal structure of Mercury's core inferred from magnetic observations

I. Wardinski[1,2], H. Amit[2], B. Langlais[2]& E. Thébault[3]

[1]Institut de Physique du Globe de Strasbourg, Université de Strasbourg/EOST, CNRS, UMR 7516,

Strasbourg, France

[2]Laboratoire de Planétologie et Géodynamique, Université de Nantes, Université d'Angers , CNRS, UMR

6112, Nantes, France

[3]Université Clermont Auvergne, CNRS, IRD, OPGC, LMV, Clermont-Ferrand, France

Key Points:

- We model Mercury's internal magnetic field from MESSENGER data with spherical harmonics
- Our core field model contains non-axisymmetric features from which we make inferences of Mercury's internal structure.
- We estimate Mercury's inner core radius of ∼500-660 km and a corresponding thickness of a top stratified layer of ∼880-500 km.

Corresponding author: I. Wardinski, `wardinski@unistra.fr`

Abstract

Previous models of Mercury's core magnetic field based on high altitude data from first MESSENGER flybys revealed an axisymmetric. Here we use low altitude MESSENGER data covering the entire mission period to construct spherical harmonic models based on various spatial norms. Although we find a dominantly axisymmetric field, our models nevertheless include detectable deviations from axisymmetry. These non-axisymmetric features appear at high latitudes, resembling intense geomagnetic flux patches at Earth's core-mantle boundary. Based on this core field morphology, we then attempt to infer Mercury's internal structure. More specifically, assuming that Mercury's high-latitude non-axisymmetric features are concentrated by downwellings at the edge of the planet's inner core tangent cylinder, and accounting for the presence of a stably stratified layer at the top of Mercury's core, we establish a relation between the inner core size and the thickness of the stratified layer. Considering plausible ranges, we propose that Mercury's inner core size is about 500-660 km, which corresponds to a stratified layer thickness of 880-500 km, respectively.

1 Introduction

Based on Mariner and MESSENGER satellite missions, it was found that Mercury's internal magnetic field is very weak, dipole dominated, largely axisymmetric and with a magnetic equator shifted northward with respect to the geographic equator at mid-latitudes of the northern hemisphere (Ness et al., 1974; Ness, 1979; Anderson et al., 2011, 2012; Johnson et al., 2012; Oliveira et al., 2015; Thébault et al., 2018; Wardinski et al., 2019), which is challenging to explain in terms of core structure and dynamics. In addition, several studies of Mercury's interior based on analyses of MESSENGER gravity field measurements and libration data suggested that the top of Mercury's outer core is thermally stratified (Smith et al., 2012; Dumberry & Rivoldini, 2015). Likely, this layer is comprised of FeS, but its phase (liquid or solid) remains uncertain. Thermal stratification implies that the heat flux at the core surface is sub-adiabatic, which has important implications for the inner core solidification and the magnetic field generation.

Numerical dynamo simulations may provide further insight into Mercury's core structure. Possible scenarios include deep-seated dynamos below a thick stable layer (Christensen, 2006; Christensen & Wicht, 2008; Takahashi et al., 2019), thin-shell dynamos (Stanley et al., 2005) and dynamos with a thin stratified layer (Stanley & Mohammadi, 2008).

The weakness of Mercury's core field motivated modeling a sulfur-rich liquid core with different zones of Fe-precipitation, i.e. iron snow. These zones could exist at the bottom of the liquid core or at the mid range between the inner and outer core boundaries (Vilim et al., 2010). While numerical dynamos with a stably stratified layer at the top of the shell can explain Mercury's weak magnetic field and its axisymmetry, additional ingredients are needed to explain the northward shift of the magnetic equator. Numerical dynamos with imposed heterogeneous heat flux in the form of equatorial cooling at the outer core boundary (Cao et al., 2014) lead to a convective instability and an offset of the magnetic equator, but their magnetic fields are too energetic and non-axisymmetric. In contrast, Tian et al. (2015) imposed a degree-1 axially heterogeneous heat flux on a dynamo model with a stratified layer at the top of the shell and hyper-diffusivity to obtain more Mercury-like magnetic fields. In both cases the validity of the results relies on the actual pattern of thermal heterogeneity at the base of Mercury's mantle, which is largely uncertain. Double diffusive convection phenomena have also been considered to explain Mercury's magnetic field. These phenomena occur when the convection is driven by two sources of buoyancy, i.e. temperature and composition (Manglik et al., 2010). Recently, Takahashi et al. (2019) showed that a double-diffusive convecting shell surrounded by a thick thermally stably stratified layer can generate Mercury-like magnetic fields. Furthermore, numerical dynamo models of Mercury's magnetic field provide estimates of the size of Mercury's inner core. Cao et al. (2014) suggested an inner core radius smaller than 1000 km. Based on geodetic analyses Dumberry and Rivoldini (2015) gave an upper limit on the inner core size of 650 km, with the outer core dynamics partly consisting of snow formation.

These different scenarios of Mercury's dynamo lead to characteristics that should be testable by observations of space-borne magnetometers like MESSENGER and Bepi-Columbo. A careful processing and analysis of magnetic field measurements taken in planetary environments is crucial for the identification of such magnetic field characteristics.

Mainly, two techniques have been applied to study Mercury's magnetic fields: potential field methods such as spherical harmonics (Uno et al., 2009; Wardinski et al., 2019), spherical caps (Thébault et al., 2018) or equivalent source dipoles (Oliveira et al., 2015) that restrict the analysis to those observations obtained in a source free region, and (reduced) parametric models that infer the magnetic dipole moment from the space probe's magnetic equator crossing, i.e. where the radial field B_r is zero, far from the planet (An-

derson et al., 2012; Johnson et al., 2012). The latter method provides models with a reduced set of parameters and is popular because of its relative independence of the data distribution. Data used for these reduced parametric models sampled the magnetic field in the magnetospheric region, with a considerable electrical current density that requires additional assumptions about the geometry and distribution of local current systems (Connerney & Ness, 1988). In contrast, Uno et al. (2009) showed by inverting synthetic data from numerical dynamo simulations that a spherical harmonic analysis can recover the large-scale magnetic field from hemispherical uneven data distribution, as single MESSENGER flybys, when data are taken in a source-free region. The resolution of finer details of the magnetic field needs, off course, numerous orbital tracks.

In this study magnetic field data are used to derive field models that may constrain the internal structure of a planet. The downward continuation of a magnetic field model to the core surface reveals patterns of magnetic flux. In particular, the latitude at which intense flux patches are concentrated may indicate the size of the inner core. Intense flux concentrations near the intersection of the inner core tangent cylinder are prominent in the geomagnetic field for at least the last 400 years (e.g. Jackson et al., 2000) and possibly over the past tens of millennia (see Panovska et al., 2019, and references therein). Numerous studies explored the kinematics as well as the dynamical origin of intense high-latitude flux patches in geomagnetic field models and numerical dynamos (Bloxham et al., 1989; Christensen et al., 1998; Amit et al., 2010, 2011; Peña et al., 2016; Olson et al., 2018). The latitude at which these flux concentrations occur has been related to the change of the dynamical regime at the tangent cylinder that is coaxial with the rotation axis and tangential to the inner core boundary (Gubbins & Bloxham, 1987), while the longitude at which these flux patches occur may be controlled by thermal core-mantle interactions (Bloxham & Gubbins, 1987).

Here we will use inferences from the Earth's core to carefully establish the relation between the latitude of intense magnetic flux patches and the tangent cylinder intersection with the core-mantle boundary (CMB), including possible errors associated with time-dependence and variability from one patch to another. We will then account for the existence of stratification to relate the depth of the stable layer with the radius of the inner core for a given latitude of magnetic flux patches. This relation will be implemented for the case of Mercury's magnetic field.

113   The aim of this study is twofold: First, we explore to what extent intermediate-
114 scale spatial features of Mercury's magnetic field can be retrieved from the MESSEN-
115 GER data by applying a spherical harmonic analysis; Second, we aim to infer the inter-
116 nal structure of Mercury's core and the convective state of its dynamo. The paper is or-
117 ganized as follows: The description of the data and their selection is given in section 2,
118 section 3 briefly describes the spherical harmonic modeling method, and results are pro-
119 vided in section 4. Implications for the generation of Mercury's core field and the struc-
120 ture of its core are discussed in section 5. We summarize our main findings in section
121 6.

2 Data selection

123   The MESSENGER spacecraft was in orbit around Mercury from 18 March 2011
124 to 30 April 2015. The orbit of MESSENGER was highly eccentric, with periapsis rang-
125 ing from 200 to 500 km over the north polar region, and apoapsides of > 12700 km above
126 the southern hemisphere. This highly eccentric orbit led to an uneven data distribution,
127 where only measurements over the northern hemisphere are assumed to be inside the mag-
128 netospheric cavity which allow adequate modeling of Mercury's internal magnetic field
129 (Oliveira et al., 2015). All local times are covered within 88 (terrestrial) days.

130   Here, we selected data from a satellite altitude range of 300 to 1000 km during lo-
131 cal night-time. The night-time selection criterion is often used in the derivation of ge-
132 omagnetic field models that are based on satellite data (Finlay et al., 2016; Lesur et al.,
133 2008; Olsen et al., 2006). This has proven to provide data sets with largely removed ex-
134 ternal field contamination and to allow a precise description of Earth's core field to high
135 spherical harmonic degrees. To this aim, we apply the same selection criterion to the MES-
136 SENGER data set. The altitude selection criterion guarantees that the analyzed mag-
137 netic field measurements are within the magnetospheric cavity: 1000 km is smaller than
138 the averaged subsolar distance of the magnetopause location (Winslow et al., 2013; Thébault
139 et al., 2018), while the lower limit excludes data from the beginning and the end of the
140 MESSENGER mission. Oliveira et al. (2019) showed that the crustal magnetic signal
141 is small-scale, and weak in amplitude at 40 km altitude. Therefore, at 300 km altitude
142 signals due to crustal magnetization are assumed to be negligible at large length scales.
143 The combination of both criteria provides a data set which shows no crustal magnetic

144 signatures and the least contamination from magnetospheric and exospheric magnetic

145 fields (Wardinski et al., 2019), which are strong at the planet's day-side.

146 **3 Method**

147   All of the selected data over the northern hemisphere (see section 2) sampled Mer-

148 cury's magnetic field in a region with almost no magnetic sources. Therefore, a poten-

149 tial theory and spherical harmonic analysis provides adequately a seperation between

150 external and internal magnetic field sources. We seek to fit MESSENGER observations

151 of Mercury's magnetic field by a potential that is parameterized using spherical harmon-

152 ics, i.e.

$$
\begin{aligned}
V = a \sum_{l=1}^{L_{\mathrm{int}}} \sum_{m=0}^{l} & \left\{ (g_l^m \cos(m\phi) + h_l^m \sin(m\phi)) \left(\frac{a}{r}\right)^{l+1} P_l^m(\cos\theta)) \right\} \\
& + a \sum_{l=1}^{L_{\mathrm{ext}}} \sum_{m=0}^{l} \left\{ (q_l^m \cos(m\phi) + s_l^m \sin(m\phi)) \left(\frac{r}{a}\right)^{l} P_l^m(\cos\theta) \right\},
\end{aligned}
\tag{1}
$$

153 where a is Mercury's radius (2440 km). r is the radial distance from Mercury's center,

154 θ the colatitude and ϕ the longitude. $P_l^m(\cos\theta)$ are the Schmidt semi-normalized asso-

155 ciated Legendre functions, where l is the degree and m the order. L_{int} and L_{ext} are the

156 truncation degrees of the spherical harmonic expansions for the internal and external field,

157 respectively. The Gauss coefficients $\{g_l^m, h_l^m\}$ and $\{q_l^m, s_l^m\}$ represent the internal and

158 external magnetic field, respectively. These model parameters are estimated by a least

159 squares fit to data collected during a given time interval. In the following, we outline de-

160 tails of our modeling technique, which is sometimes called smoothed inversion (Holme

161 & Bloxham, 1996; Uno et al., 2009). From the selected data, we derive models with $L_{\mathrm{int}} =$

162 10 and $L_{\mathrm{ext}} = 1$. External magnetic fields of higher spherical harmonic degrees can-

163 not be estimated with confidence by using a regularized inversion. Their signals should

164 contribute to the model residuals, i.e. un-modeled signals. These un-modeled signals could

165 be partly related to the magnetic signatures of Birkeland currents, which mainly exist

166 in the dawn and dusk sections of the data local times at latitudes higher than 70° North.

167 Their signals are generally in the horizontal field components, with magnitudes of only

168 20 nT and they do not rotate with the planet (Anderson et al., 2018).

¹⁶⁹ **3.1 Model priors**

¹⁷⁰ For a linear least squares problem the model vector m containing the Gauss coef-

¹⁷¹ ficients is found at the minimum of an objective function

$$\Theta(m) = (\mathsf{y} - \mathbf{A}\mathsf{m})^{\mathsf{T}}\mathbf{C_e}^{-1}(\mathsf{y} - \mathbf{A}\mathsf{m}) + \lambda_S(\mathsf{m}^{\mathsf{T}}\mathbf{C_m}^{-1}\mathsf{m}), \tag{2}$$

¹⁷² where y is the data vector, $\mathbf{A}$ a design matrix, $\mathbf{C_e}$ the data error covariance matrix and

¹⁷³ $\mathbf{C_m}$ the prior model covariance matrix (Jackson, 1979; Gubbins, 1983) which is controlled

¹⁷⁴ by a Lagrange multiplier (λ_S). The misfit of the model is computed by

$$\hat{\sigma} = \sqrt{\frac{\sum_{i=1}^{N}(y_i - \hat{y}_i)^2}{N - 1}}, \tag{3}$$

¹⁷⁵ where $\hat{y}_i$ is the model value for given observation y_i.

¹⁷⁶ Our method to find the Gauss coefficients utilizes prior constraints to reduce the

¹⁷⁷ ambiguity of the data inversion. The application of priors to constrain the inversion of

¹⁷⁸ MESSENGER data to obtain a model of Mercury's magnetic field is justified by their

¹⁷⁹ uneven hemispherical distribution. Primarily, the prior should emphasize the large-scales

¹⁸⁰ of Mercury's magnetic field. We test the performance of four different priors of the spa-

¹⁸¹ tial complexity of the model's field morphology. These priors are usually formulated as

¹⁸² model norms:

$$\text{Norm}\,1 : \oint B^2 dS|_{r=c} = (l+1)\left(\frac{a}{c}\right)^{(2l+4)}$$

$$\text{Norm}\,2 : \oint B_r^2 dS|_{r=c} = \frac{(l+1)^2}{2l+1}\left(\frac{a}{c}\right)^{(2l+4)}$$

$$\tag{4}$$

$$\text{Norm}\,3 : \oint (\nabla_h B_r)^2 dS|_{r=c} = \frac{l(l+1)^3}{2l+1}\left(\frac{a}{c}\right)^{(2l+6)}$$

$$\text{Norm}\,4 : \oint F dS|_{r=c} = \frac{(l+1)(2l+1)(2l+3)}{l}\left(\frac{a}{c}\right)^{(2l+3)} \leq Q.$$

¹⁸³ In Norm 4 of (4) F is the field intensity and Q is the mean CMB heat flux. In all these

¹⁸⁴ expressions (4), Mercury's core radius is $c = 2060$ km (Wardinski et al., 2019). Norm

¹⁸⁵ 1 minimizes the power of the magnetic field for higher spherical harmonic degrees, and

¹⁸⁶ therefore it steepens the slope of its power spectrum. Norms 2 and 3 smooth the radial

¹⁸⁷ magnetic field and its horizontal gradient, respectively (Shure et al., 1982). Norm 4 is

¹⁸⁸ different from the other norms as it may include prior knowledge of the heat flux at Mer-

¹⁸⁹ cury's core surface, which is due to the Ohmic dissipation of the radial field B_r at the

¹⁹⁰ core surface (Gubbins, 1975). However, there are no observations of the heat flux at Mer-

¹⁹¹ cury currently available. Therefore, Norm 4 acts merely as a constraint to stabilize the

solution of the inversion like the other norms. All norms dim the amplitude of small-scale field features, though at different ways, hence support the large-scale morphology of the magnetic field. Among these norms, this effect is most strongly imposed by Norm 3, where the attenuation scales with l^3.

The resulting model is determined by varying the strength of the prior to be in optimal balance between data misfit and model smoothness. This optimal balance is usually found for the λ_S at the knee of their trade-off or L-curves.

3.2 Iterative modeling scheme

To find the model parameters, we adopt an iterative re-weighting scheme that consists of three steps. At a first step, we determine a model that is based on data covering the MESSENGER's entire mission interval at Mercury. Data are weighted equally, to form the initial error covariance matrix, $\mathbf{C_e}$, in (2). We assign an initial error of 1.6 nT to each datum which corresponds to the upper limit of the instrument's resolution (Anderson et al., 2007). At a second step, individual differences between each data and corresponding values of the initial model are computed, to provide an update of $\mathbf{C_e}$ and, third, to derive the final model with the updated error covariance matrix. The residual amplitude, and therefore $\mathbf{C_e}$, depends directly on the Lagrange multiplier λ_S; In order to obtain a close trade-off curve for each norm, this iterative re-weighting scheme is applied for each setting of λ_S. In total we derive a large number of models for each norm. We select the model at the knee of each norm trade-off curve.

A closer inspection of the residuals reveals anomalous tracks that show significant larger residual amplitudes than others. The cause for these large residuals remains unclear, but could be related to instrument errors and/or data processing errors. However, these data are automatically down-weighted and rejected from the model derivation when the misfit is larger than $2\,\sigma$.

3.3 Robustness of the solutions

There are a few diagnostics to evaluate the robustness and confidence of the inversion results. First, we analyze the resolution matrix of the model m, to obtain a measure of model parameter significance. The resolution matrix is given by

$$\mathbf{R} = (\mathbf{A}^\mathsf{T}\mathbf{C_e}^{-1}\mathbf{A} + \lambda_s\mathbf{C_m}^{-1})^{-1}\mathbf{A}^\mathsf{T}\mathbf{C_e}^{-1}\mathbf{A}\,, \qquad (5)$$

Table 1. Inversion parameters, diagnostics and global characteristics of the field models.

	Norm1	Norm 2	Norm 3	Norm 4
λ_s	8.0×10^2	8.0×10^2	4.0×10^2	8.0×10^6
rms misfit (nT)	26.11	26.09	26.5	26.39
Trace of R-Matrix	65	70	36	57
rms field intensity (nT)	331.19	332.75	327.05	335.24
g_1^0 (nT)	-217.5	-218.8	-213.8	-221.5
g_2^0/g_1^0	0.29	0.29	0.31	0.28
dipole tilt angle (°)	0.6	0.4	0.7	0.8

where the diagonal elements of $\mathbf{C_m}$ are defined in (4). Ideally, this matrix would be an identity matrix. Due to inadequacy of the data, a regularization scheme must be applied in the solving process to obtain a stable solution. This is reflected in the form of the resolution matrix. A value of the resolution near 1 means that a model parameter is wholly determined by the data, whereas a low resolution, i.e. values ~ 0.1, means that the model is mostly controlled by the prior information. The trace of the resolution matrix $Tr(\mathbf{R})$ can be broadly interpreted as the degree of freedom of the model and as the number of model parameters resolved by the inversion (Tarantola, 1987).

Characteristics and diagnostics of the field models are listed in Table 1. All models widely agree in their statistical properties, and mostly differ in their numbers of resolved parameters. The lowest number of resolved parameters is found for Norm 3, as it more strongly damps contributions of higher spherical harmonic degrees than other norms and therefore reduces the degree of freedom most strongly.See appendix B for a further discussion of the inversion covariance matrix.

4 Results

In this section, we present models of Mercury's time-averaged magnetic field as they are based on MESSENGER measurements covering the period 2011-2015. We discuss to what extent our results are conclusive and estimate their robustness. The models provide reasonably good fits to the data with residuals of $\sim$8% of the total field strength.
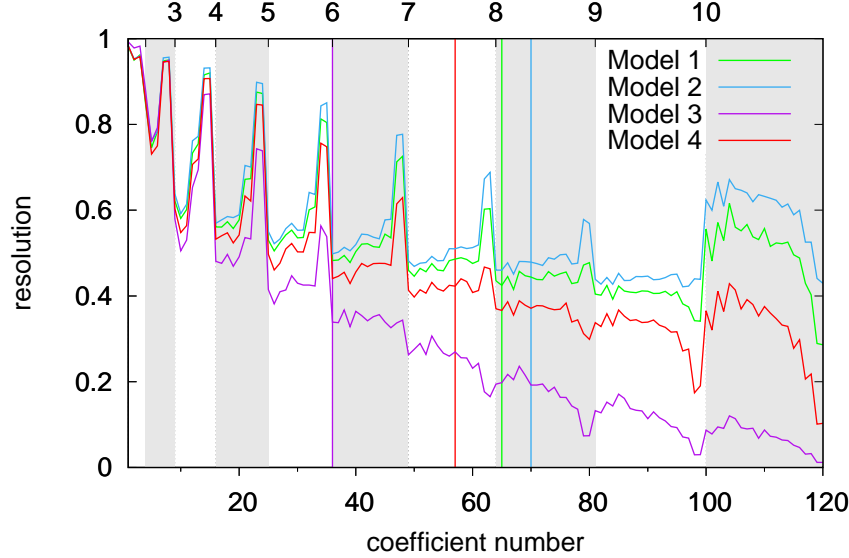
Figure 1. Diagonal elements of the resolution matrix of the preferred models for different priors vs. coefficient number (see also degree at the top axis). Gray shaded areas indicate even spherical harmonic degrees. The colored vertical lines represent the degree of freedom of the respective model.

4.1 Resolution analysis and spectral content

For each of the four resulting models we computed the resolution matrix $\mathbf{R}$, and charted their diagonal elements, where labels of the models refer to the norm used to constrain the solution, e.g. Norm 1 → Model 1. These plots (resolution curves) are shown in Figure 1.

The resolution curves of all models generally agree for the first four spherical harmonic degrees. Most notable are the high resolution of sectorial Gauss coefficients, i.e. g_m^m, h_m^m, of at least the first five spherical harmonic degrees. Resolution curves of models 1, 2 and 4 show this particular pattern also for higher spherical harmonic degrees, which may indicate a higher ability of these norms to capture small-scale magnetic field signatures. The higher resolution of the sectorial terms could also be explained by MESSENGER's flight path along latitude. We find that Model 3 resolves magnetic field structures only until spherical harmonic degree 5. Model 4 partly resolves spherical harmonic degree 7, whereas Models 1 and 2 show a higher resolution and partly resolve degree 8. Vertical lines in Figure 1 mark the maximum number of resolved model parameters cor-

255 responding to the trace of the resolution matrix (see Table 1). This coincides with a res-

256 olution level of ∼ 0.4. Below this level, the model is assumed to be dominated by the

257 prior. At degree 10, i.e. coefficient numbers between 100 and 120, Models 1, 2 and 4 show

258 an enhanced resolution, where they may become sensitive to spectral leakage, signals of

259 other sources and possible data errors. We assume the high resolution at these small scales

260 to be an artifact and possibly caused by the orbital geometry of MESSENGER. Holme

261 and Bloxham (1996) discussed a similar effect observed in the Voyager II data at Nep-

262 tune, which was likely caused by the spacecraft trajectory. The setting of a maximum

263 degree L_{int} for the spherical harmonic expansion leads also to an aliasing of the higher

264 degree field ($l > L_{\text{int}}$) into coefficients of the model spherical harmonic expansion (spec-

265 tral leakage).We assume this effect to be reduced by truncating the models to spherical

266 harmonic degree $L_{\text{int}} = 8$.

267 Maps derived from truncated models ($l = 8$) of the radial magnetic field at the

268 core surface are shown in Figure 2. As expected field structures in the northern hemi-

269 sphere show more details than in the southern hemisphere, because of the data distri-

270 bution. Generally, the field is dominated by the axial dipole, but the magnetic equator

271 is significantly shifted towards the North pole in agreement with previous studies (An-

272 derson et al., 2011, 2012; Thébault et al., 2018). The different models show differing spa-

273 tial complexities, in particular of the magnetic equator. The map derived with Norm 3

274 shows the most axisymmetric field morphology, whereas models derived with Norms 1

275 and 2 show more longitude-dependent structures including even some reversed flux patches.

276 Overall, all models tend to agree in their large-scale structure (Table 1) and differ in their

277 quantification of small scale features.

278 All models (1 - 4) show axial quadrupole-dipole ratios of 0.28-0.31 (Table 1) which

279 are significantly smaller than those obtained by dipole offset models (Anderson et al.,

280 2012; Johnson et al., 2012) but are in agreement with a model constructed using spher-

281 ical caps (Thébault et al., 2018). We note that we could force the models to have a larger

282 quadrupole-dipole ratio close to $g_2^0/g_1^0 = 0.4$ (found by Anderson et al. (2012); John-

283 son et al. (2012)); however, this leads to 10 - 20% larger rms misfits, which we consider

284 to be significant and eventually deleterious for a large quadrupole-dipole ratio.

285 Maps in Figure 2 have also structures where no data are available, i.e. in the south-

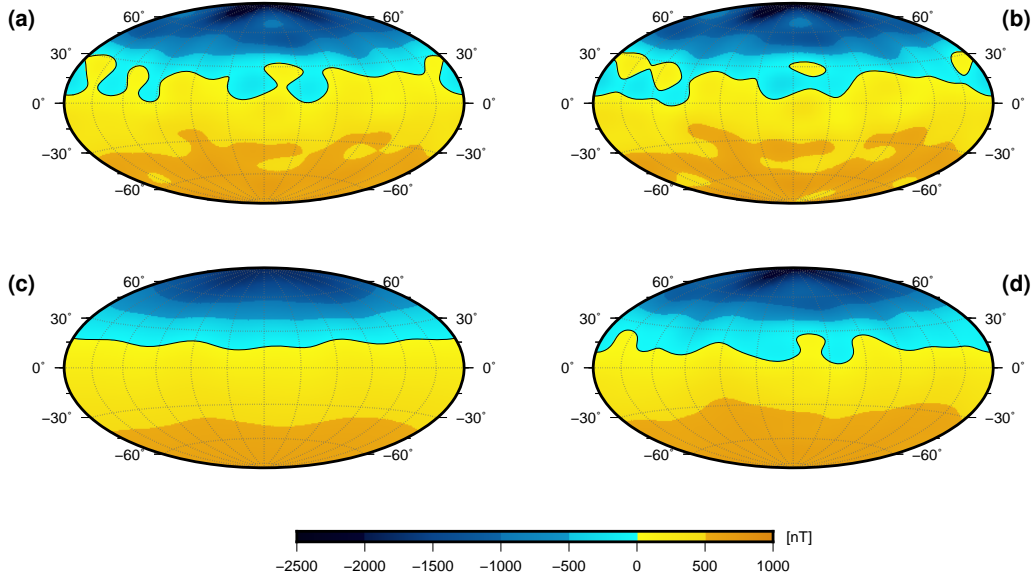286 ern hemisphere. The magnetic field morphology in this hemisphere is mostly determined

Figure 2. Radial component of the magnetic field at Mercury's core surface of the selected model solutions: (a) Model 1, (b) Model 2, (c) Model 3 and (d) Model 4.

by the global characteristic of the spherical harmonic analysis and the prior used in the inversion. We, therefore do not attempt to interpret magnetic field features in the southern hemisphere.

Power spectra (Lowes, 1966; Mauersberger, 1956) of the models at the core surface are shown in Figure 3. The spectra mostly match for spherical harmonic degrees 1 to 3. We find three different types of spectral slopes for spherical harmonic degrees $l >$ 5: decreasing, increasing and flat. The spectral power of Model 3 drops exponentially, whereas Models 1 and 2 show powers that increase by one order of magnitude. Model 4 shows a flatter spectrum. This may lead to similar conclusions as taken from the resolution analysis, where for Models 1, 2 and 4 spherical harmonic degrees above $l > 8$ may be influenced by spectral leakage of magnetic small-scale sources close to the surface of Mercury.

Common characteristics of all models are represented by their median of the models. This technique is commonly used in the derivation of the International Geomagnetic Reference Field model (IGRF), where a wide variety of geomagnetic main field models based on diverse modeling philosophies are averaged (Thébault, Finlay, Alken, et al., 2015). The discussion of the spatial characteristic of Mercury's time-averaged magnetic field will
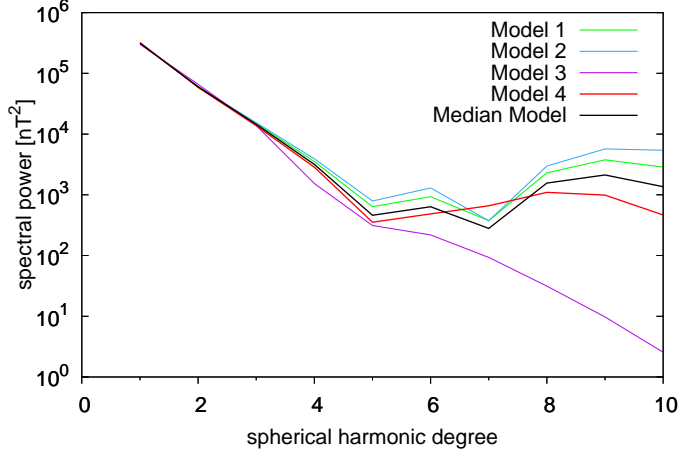
Figure 3. Power spectra of the magnetic field models at Mercury's core surface.

therefore be based on this median model which neither should be too damped (as Model 3) nor too contaminated by spectral leakage at high spherical harmonic degrees (as probably Models 1 and 2). As mentioned earlier (see discussion of Figure 1), we are not convinced by the robustness of spherical harmonic degrees 9 & 10, and therefore we truncate the median model to spherical harmonic degree 8.

4.2 Mercury's time-averaged magnetic field

Maps in Figure 4 are derived from the median model until spherical harmonic degree 8. Figures 4a and b show the non-dipole field and the non-axisymmetric, i.e. non-zonal, field at Mercury's core surface, respectively. The mapping of the non-dipole field excludes the dipole coefficients g_1^0, g_1^1 and h_1^1, whereas the non-axisymmetric field excludes all zonal terms, i.e. g_l^0. The non-dipole field (Figure 4a) is dominated by the equatorial-symmetric g_2^0 term. Though the estimate of g_2^0 is strongly influenced by the uneven distribution of MESSENGER data, it is the second strongest coefficient of the field. In addition, the field features at the northern hemisphere are stronger due to significant equatorial-antisymmetric terms, i.e. g_3^0. Finally, the signature of two normal polarity flux patches at northern high latitudes is evident in Figure 4b. Recall that Figure 4b shows the non-zonal field; the two negative structures correspond to two normal polarity flux patches, while the two positive non-zonal structures are the lows in between (see Figure 4a).

The polar view map of the non-dipole radial field at the surface of Mercury's core (Figure 4c) shows an elongated patch of intense magnetic flux over the North pole. This
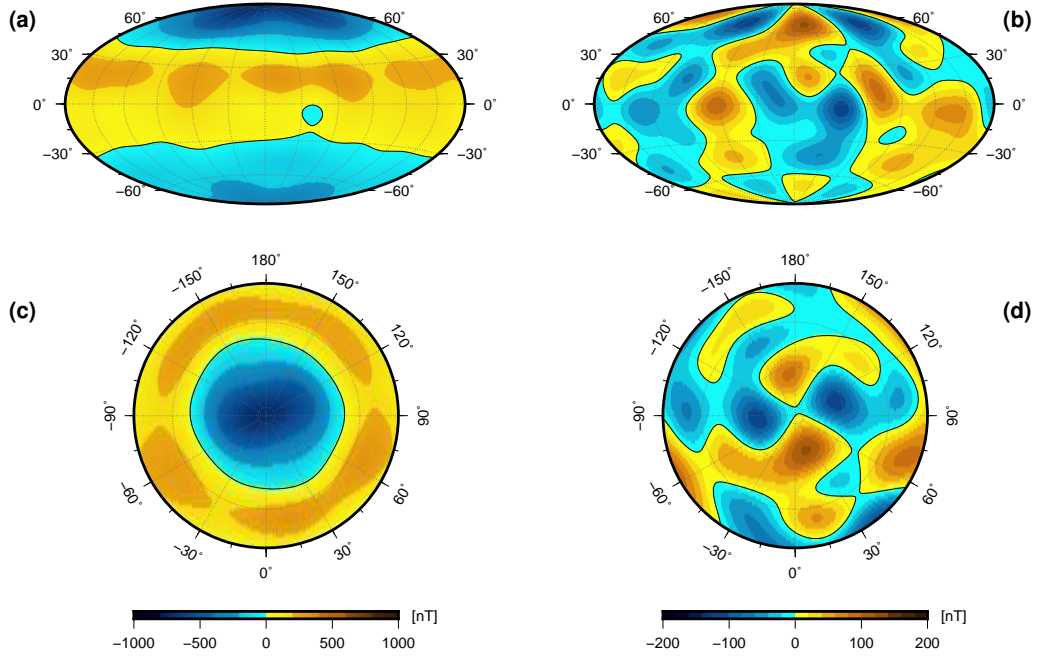
Figure 4. Radial component of: (a) the non-dipole and (b) the non-axisymmetric (non-zonal) magnetic field at Mercury's core surface, respectively. (c) and (d) show north polar views of these magnetic field parts. Maps are derived using the median model truncated at spherical harmonic degree $L_{\rm int} = 8$. The black lines mark the zero contour. Note different scales for maps (a), (c) and (b), (d).

pattern is surrounded by a region of positive (i.e. opposite polarity) magnetic flux with some intensified patterns, where the boundary between these regions of opposite polarity, i.e. the magnetic equator (black line) shows considerable undulations. These undulations further indicate non-axisymmetric field contributions.

The non-zonal field, shown in Figures 4b and d, is fainter. Its amplitude ranges between $\pm$ 200 nT, corresponding to $\sim$ 15% of the total field. This part of the field allows to unravel longitude-dependent structures that are otherwise masked by the strong axisymmetric field. Particularly, the non-zonal field shows four features with alternating signs at high latitudes (A, B, C & D in Figure 5), indicative of two intense normal flux patches. The centers of these flux patches appear approximately at 65° northern latitude.

Furthermore, Mercury's core field also shows non-zonal structures at lower latitudes. These primed features (A', B', C' & D' in Figure 5) are weaker than their higher latitude counterparts. The primed features seem to be shifted relatively to the higher latitude structures by a longitudinal angle of 30° to 60° to the west. The very existence of the primed features may provide further interpretations of processes and structures within Mercury's core. However, their relative weakness might render these interpretations as too speculative.

The primed and un-primed features are not related to magnetic signatures of Birkeland currents that are flowing in the north polar region for several reasons. First, because the magnetic field of Birkeland currents is most prominent in the horizontal directions, i.e. it is and absent in the radial component; Birkeland currents flow in radial direction, consequently their induced magnetic field is horizontal. Secondly, their signatures would occur as an auroral band in a time-averaged analysis. The auroral band has a zonal structure which is removed from maps of the non-zonal B_r, i.e. in Figures 4b, 4d and 5. Finally, the amplitude of features A, B, C & D is about 5 times larger than the magnetic signal of Birkeland currents.

4.3 Inferring Mercury's internal structure

The concentric arrangement of non-zonal features (A, B, C & D) in the northern hemisphere as seen in Figure 5 could be indicative of processes that are involved in the magnetic field generation. To reach conclusions about these processes, we assume that
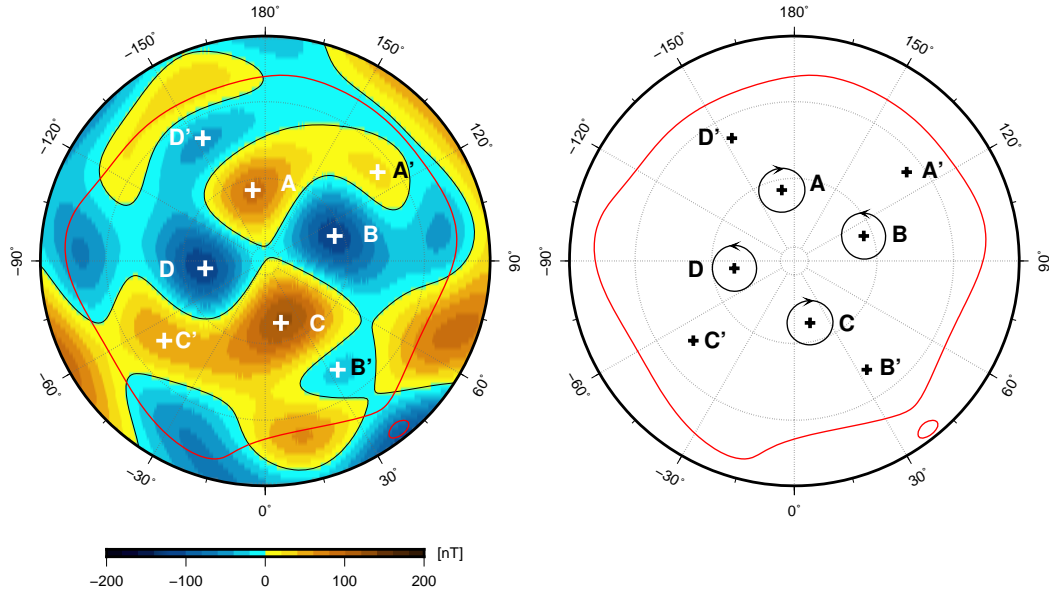
Figure 5. Polar view of the non-axisymmetric radial magnetic field at Mercury's core surface. The red line shows the position of the magnetic equator, capital letters mark apparent non-zonal field features and pluses their centers. Right: a schematic illustration of the individual convective rolls associated with the high-latitude non-zonal field features (clockwise A, C; counterclockwise B, D).

355 the nature of these features are linked to columnar rolls tangent to the inner core, par-

356 allel to the planet's spin axis i.e. these columnar rolls are expected to be equatorially

357 symmetric. Busse (1975) showed that such columnar flow exists when the Coriolis force

358 dominates viscous and Lorentz forces in the convective region. Oppositely rotating con-

359 vective rolls (clockwise and anticlockwise, see Figure 1 of Busse, 1975) may explain the

360 different signs of the non-zonal magnetic field structures. Cyclones/anti-cyclones in the

361 northern hemisphere correlate with convergence/divergence and concentrated/dispersed

362 field, respectively (e.g. Olson et al., 1999)). Accordingly, in Figure 5 the flux patches B

363 & D may be concentrated by fluid downwellings associated with cyclones, while the pos-

364 itive non-zonal field (i.e. relatively weak field) in A & C may be dispersed by fluid up-

365 wellings associated with anti-cyclones.

366 We interpret the latitude of these flux patches by comparing them to Earth's mag-

367 netic core field. Amit et al. (2011) quantitatively identified centers of geomagnetic in-

368 tense flux patches. Their Figure 9 and our Figure A.1 suggest that patch centers appear

369 persistently at latitudes somewhat lower than that of the tangent cylinder. Analysis of

370 the *gufm1* historical geomagnetic field model (Jackson et al., 2000) reveals that patch

371 latitudes are time-dependent, appearing from about $30°$ latitude lower than the tangent

372 cylinder until very close to it. However, in recent epochs when the field models are more

373 reliable the patches reside less than $\sim 10°$ lower than the tangent cylinder (Amit et al.,

374 2011). This agrees with our analysis of a recent IGRF model (Thébault, Finlay, Beggan,

375 et al., 2015). The latitude of the geomagnetic flux patches based on Figure A.1 is ap-

376 proximately $8°$ lower than that of the tangent cylinder. We conclude that based on the

377 behavior of the geomagnetic field the offset between the patches and the actual latitude

378 where the tangent cylinder intersects the CMB is roughly $\delta\theta \sim 10° \pm 10°$.

379 Figure 6 (top) illustrates the classical tangent cylinder geometry with the addition

380 of the effect of $\delta\theta$. This geometry is written as

$$\sin(\theta_{cmb} - \delta\theta) = \frac{r_i}{r_o}, \tag{6}$$

381 where r_i and r_o are the radii of the inner core and the CMB respectively. We assume

382 that θ_{cmb} can be obtained from Mercury's non-zonal field and that $\delta\theta$ is similar to Earth's

383 value. This allows to derive r_i, Mercury's inner core size. However, the presence of a strat-

384 ified layer at the top of the core complicates this inference. When such a layer exists, the

385 convective rolls concentrate flux at the base of the stratified layer, from which a skin ef-
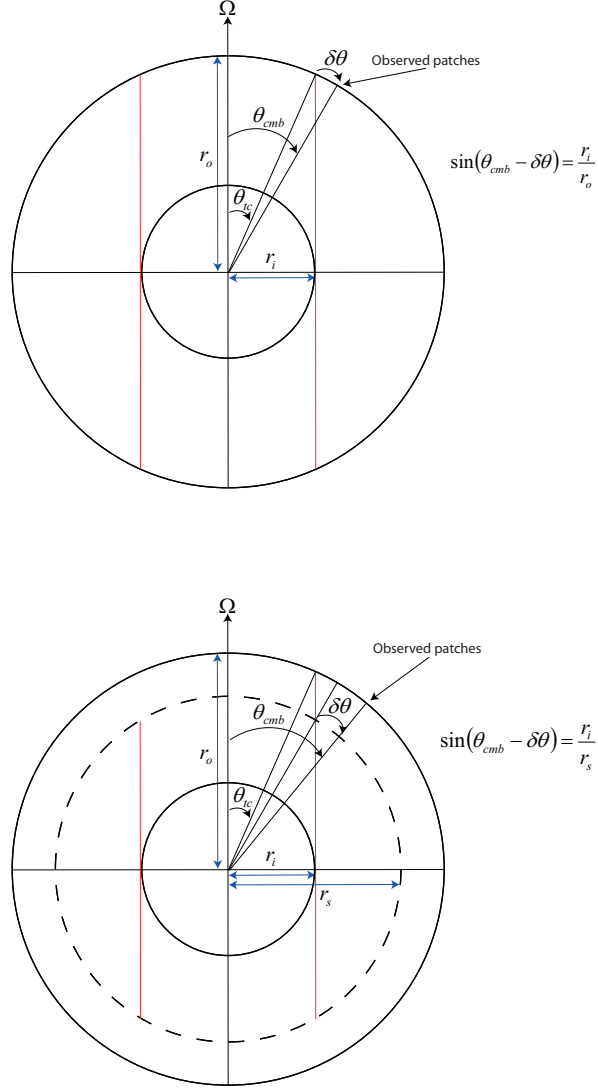
Figure 6. Schematic illustrations of the geometry of the tangent cylinder effect without (top) and with (bottom) a stably stratified layer. See text for the definitions of different angles.

fect may carry the signal to the CMB by diffusion (Christensen, 2006; Christensen & Wicht, 2008). The presence of zonal flows in the stratified layer (Olson et al., 2018; Christensen, 2018) might complicate our inference of the core structure, though these flows would advect the magnetic flux patches in the east-west direction with a lesser impact on their latitudes which is the focus of our analysis.

Assuming that the signal propagation across the stratified layer is roughly radial, then Figure 6 (bottom) illustrates the relation between the co-latitude of the patches θ_{cmb}, the radius of the inner core r_i and the radius of the base of the stratified layer r_s. Mathematically this relation is

$$\sin(\theta_{cmb} - \delta\theta) = \frac{r_i}{r_s}, \tag{7}$$

which contains two unknowns, r_i and r_s, and therefore cannot be uniquely determined. However, it provides a useful constraint and may be used to highlight various plausible scenarios for Mercury's internal structure.

To estimate Mercury's inner core size, we first estimate θ_{cmb} from Mercury's magnetic field model. The centers of intense flux patches B & D (Figure 5) reside at about latitude $\sim 65°$ North, or co-latitude $\theta_{cmb} = 25°$. From the analysis of the geomagnetic field we further assume $\delta\theta = 10° \pm 10°$. Substituting these values into (7) gives scenarios for Mercury's internal structure. Figure 7a presents the results for Mercury's inner core size r_i and the thickness of the convective region is given in Figure 7b. Both are functions of the radius of the base of the stratified layer r_s, for three values of $\delta\theta$ which cover the considered range. Small values of r_s, which correspond to a very deep base of the layer (thick layer), give a very small inner core which would render the production of non-zonal features at the base of the stratified layer and hence the identification of a tangent cylinder effect to be impossible. Moreover, the magnetic Reynolds number scales with the convective shell thickness; if most of the core is stratified, a dynamo action is unlikely. Larger values of r_s, which correspond to a thinner stratified layer, give a thicker inner core with stronger dependence on $\delta\theta$. For a thin stratified layer of ~ 50 km, with $\delta\theta = 0°$ we find an upper bound $r_i \sim 850$ km and a convective region of 1160 km, with $\delta\theta = 10°$ we find $r_i \sim 500$ km and a convective region of 1490 km, whereas with $\delta\theta = 20°$ r_i is ~ 180 km and a convective region of ~ 1830 km. On the other hand, with a thick stratified layer of ~ 1600 km for all $\delta\theta$ the inner core size is smaller than 200 km and the respective sizes of the active dynamo region are less than 400 km.
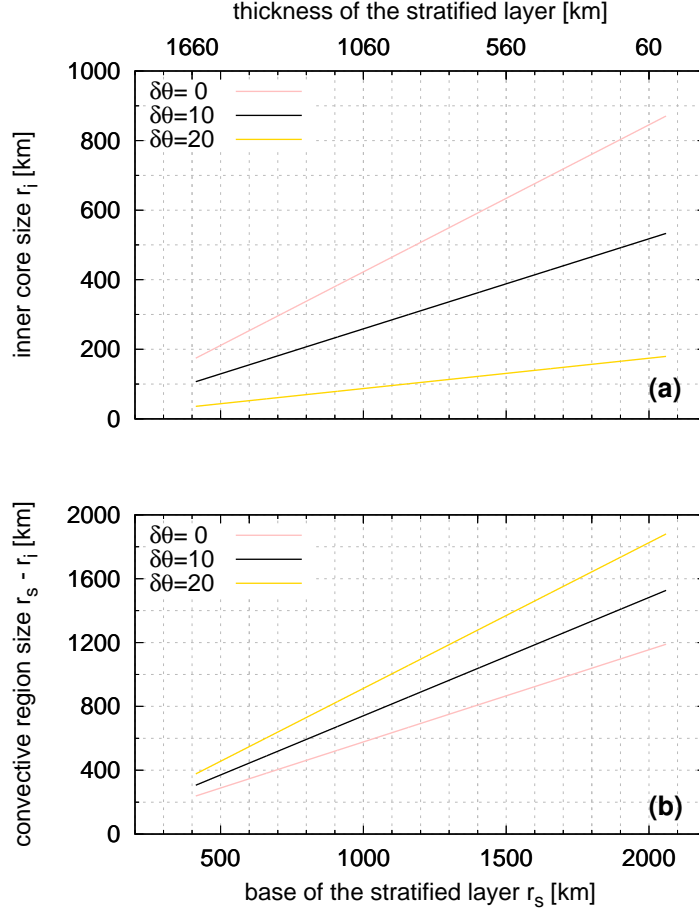
Figure 7. Mercury's inner core size r_i (a) and the thickness of the convective region (b) vs. the radius of the base of the stratified layer r_s (or the layer thickness, see top horizontal scale), for three values of $\delta\theta$ (see legend).

In the discussion section we elaborate on the consequences of the latitude of the magnetic flux patches on inferring the internal structure of Mercury.

5 Discussion

Figure 1 can directly be compared to results of a resolution analysis by Uno et al. (2009). The resolution of our preferred model is certainly higher than the resolution of their inversion results. This is mainly because of the wider spatial coverage during the MESSENGER main mission (2011 - 2015) than during the three flybys of Mariner-10 and the one MESSENGER flyby in 2008. However, Uno et al. (2009) concluded that a realistic resolution up to spherical harmonic degree 10 can be obtained from the flyby data. We consider this as an optimistic view, as it (implicitly) assumes that model pa-

427   rameters with a small but non-zero resolution can be resolved by the inversion. In this

428   respect, we are cautious in choosing a minimum resolution R_{min} which would be rele-

429   vant for robust results. We find that a value of $R_{min} \geq 0.4$ is a diligent choice for a re-

430   quired minimum resolution. The model solutions 1, 2 and 4 largely meet this criterion,

431   and maps of these models are in good agreement when truncated to spherical harmonic

432   degree $l = 8$. Small-scale structures along the magnetic equator, particularly those seen

433   in Models 1 and 2, arise from spherical harmonic degrees $l > 8$ which we consider as

434   uncertain.

435   The tangent cylinder effect is expected to hold when the dynamics is dominated

436   by rapid rotation effects. This is the case in Earth's core (e.g Jault, 2008; Aubert, 2013;

437   Long et al., 2020). However, the dynamical regime in Mercury's liquid core is largely un-

438   certain due to the unknown convection vigor there. To reproduce the magnetic equator

439   offset of Mercury's field, the dynamo models of Cao et al. (2014) exhibit a superposition

440   of two unstable columnar convection modes in rapidly rotating spheres, whereas the mod-

441   els of Takahashi et al. (2019) contain an anti-symmetric flow component. Overall, cau-

442   tion is required when considering our results which would be valid only if rapid rotation

443   effects govern Mercury's core dynamics. Bearing this in mind, our inference of the in-

444   ner core size could provide insights to characterize the planet's internal structure and

445   the dynamo action in its core. The morphology of Mercury's non-axisymmetric magnetic

446   field that is shown in Figures 4b and d exhibits two high-latitude normal flux patches.

447   The axisymmetric and non-axisymmetric parts of Mercury's magnetic field may be due

448   to different processes. In this context it has been proposed that a stratified layer out-

449   side the dynamo region of Saturn leads to the axisymmetrization of its magnetic field

450   (Stevenson, 1982; Stanley, 2010). Similar mechanisms are likely to be at work inside Mer-

451   cury (Christensen, 2006; Christensen & Wicht, 2008).

452   Mercury's internal structure is still unresolved by geodetic analyses and there is

453   a debate concerning the existence and possible size of a solid inner core. If a solid inner

454   core exists, it was argued that its radius is likely to be smaller than ∼1000 km (Van Hoolst

455   et al., 2012; Cao et al., 2014; Dumberry & Rivoldini, 2015; Peale et al., 2016). Based on

456   estimates of Mercury's gravity field, tidal Love number and pole coordinates, Mercury's

457   inner core radius is in the range 883 to 1026 km (Genova et al., 2019). However, reported

458   values of Mercury's inner core size are still under debate and estimates derived from a

geodetic analysis of Mercury's orbital motion give a larger range of 370-1200 km (from combining the first and third quartiles of Margot et al., 2018).

Based on the above estimates from geodetic analyses we consider Mercury's inner core size to be $r_i =$500-1000 km. For $r_i =$500 km and $\delta\theta = 0°$ Figure 7(a) gives a stratified layer thickness of ∼880 km which leaves ∼680 km for the convective region to maintain a dynamo. For $r_i = 500$ km and $\delta\theta = 10°$ the stratified layer thickness is ∼130 km and the convective region is ∼1430 km, while for $r_i = 500$ km and $\delta\theta = 20°$ a solution does not exist. Furthermore, an inner core size of $r_i =$1000 km is out of range for the considered $\delta\theta$ values (Figure 7(a)). Because the large scale field of Mercury favors a substantial stratified layer, and because large r_i constrains $\delta\theta$ to small admissible values, we conclude that the inner core size tends towards the small end of the considered r_i range.

The thickness of the stratified layer at the top of Mercury's core is also unknown. Smith et al. (2012) suggested that a 200 km thick and solid FeS-layer at the interface of a silicate mantle and the metallic core may explain the planet's moment of inertia. However, this setup was questioned by Hauck et al. (2013) who derived models without an FeS-layer to reproduce the gravity field observations and libration data. The thickness of such a layer depends on the available Sulfur and its solubility in the metallic core determined by the widely unknown core temperature and reduction conditions (Hauck et al., 2013). In most numerical dynamo simulations that attempt to explain observations of Mercury's magnetic field a thick layer is assumed, from several hundred km (e.g. 600 km in Christensen, 2006; Christensen & Wicht, 2008) up to half the core radius (Takahashi et al., 2019). The stratified layer weakens and diffuses the non-axisymmetric field via a skin effect, which could explain its low intensity and dominant axisymmetry.

Considering a stratified layer thickness of 500-1000 km (or $r_s =$1560-1060 km), we obtain $r_i \sim$660-90 km and a dynamo region of ∼1420-610 km, respectively with ranges corresponding to the different $\delta\theta$ values (Figure 7). The small inner core scenario (with $\delta\theta = 20°$) seems unlikely to produce a detectable tangent cylinder effect. We therefore favor again the solutions for low $\delta\theta$ which correspond here to inner core sizes of ∼660-450 km and convective region sizes of approximately 900-610 km.

6 Conclusion

In this study, we investigate the morphology of Mercury's magnetic core field and the smallest possible spatial scales that can be resolved from the MESSENGER measurements. Our spherical harmonic analysis demonstrates that features of the time-averaged magnetic core field of spherical harmonic degree $l = 8$ can be robustly resolved, independent of the model prior. Higher spherical harmonic degrees are likely aliased by undetermined magnetic signatures. Moreover, we detect non-axisymmetric features of the core magnetic field that are absent in the dipole offset model (Anderson et al., 2012; Johnson et al., 2012).

For the first time, Mercury's non-axisymmetric core field is identified and studied to infer the internal structure of its core. We find non-axisymmetric flux patches at high northern latitudes. We interpret these features as the signature of convective columns adjacent to the inner core tangent cylinder. The deviation from axisymmetry introduced by these patches is far less pronounced than at Earth's geomagnetic field due to the masking by Mercury's dominant axisymmetric field.

We take advantage of the mean latitude of these two patches to constrain Mercury's internal structure. We establish a relation between the inner core size and the thickness of the stratified layer below the CMB as a function of the latitude of the magnetic flux patches. While various combinations of these two quantities are possible, a combined interpretation of our results and those from geodetic analyses limits the range of the inner core radius to ∼500-660 km. Accordingly the stratified layer thickness is ∼880-500 km, leaving ∼900-610 km for the convective dynamo region, respectively. Furthermore, our results favor little (if any) shift between the locations of magnetic flux patches and the tangent cylinder at the top of the dynamo region, in apparent contrast to the offset observed at Earth's core.

Finally we emphasize that our analysis is based on a data set of the MESSENGER mission over the northern hemisphere only. This puts limits on the magnetic field models and the inferences concerning Mercury's internal structure. The future Bepi-Colombo mission will unravel these details of Mercury's magnetic core field.

Acknowledgments

The MESSENGER mission was supported by the NASA Discovery Program under contracts NAS5-97271 to The Johns Hopkins University Applied Physics Laboratory and NASW-00002 to the Carnegie Institution of Washington. All MESSENGER data used here are publicly available on NASA's Planetary Data System (PDS) `https://doi.org/10.17189/1519745`. This research was supported by the French Agence Nationale de la Rercherche, project MARMITE, contract 654 ANR-13-BS05-0012, as well as by Centre National des Etudes Spatiales in the context of the BepiColombo MAG experiment. Models and auxiliary files will be made available upon requests directed to the first author. We are grateful for very constructive comments by two anonymous reviewers and we would like to thank J. Wicht for suggesting to test for models with larger quadrupole-dipole ratio. All graphics were produced using opensource software, GMT(Wessel et al., 2013) and gnuplot.

The authors declare that they have no competing interests.

References

Amit, H., Aubert, J., & Hulot, G.   (2010, Jul).   Stationary, oscillating or drifting mantle-driven geomagnetic flux patches?   *Journal of Geophysical Research (Solid Earth)*, *115*(B7), B07108. doi: 10.1029/2009JB006542

Amit, H., Korte, M., Aubert, J., Constable, C., & Hulot, G. (2011, December). The time-dependence of intense archeomagnetic flux patches.   *Journal of Geophysical Research (Solid Earth)*, *116*(B12), B12106. doi: 10.1029/2011JB008538

Anderson, B. J., Acuña, M. H., Lohr, D. A., Scheifele, J., Raval, A., Korth, H., & Slavin, J. A. (2007). The Magnetometer Instrument on MESSENGER. *Space Science Reviews*, *131*(1), 417–450. doi: 10.1007/s11214-007-9246-7

Anderson, B. J., Johnson, C. L., Korth, H., & Philpott, L. C.   (2018).   Birkeland Currents at Mercury: Review and Comparison With Earth.   In A. Keiling, O. Marghitu, & M. Wheatland (Eds.), *Electric currents in geospace and beyond* (Vol. 235, p. 279-302). doi: 10.1002/9781119324522.ch17

Anderson, B. J., Johnson, C. L., Korth, H., Purucker, M. E., Winslow, R. M., Slavin, J. A., . . . Zurbuchen, T. H. (2011, Sep). The Global Magnetic Field of Mercury from MESSENGER Orbital Observations.   *Science*, *333*(6051), 1859. doi: 10.1126/science.1211001

Anderson, B. J., Johnson, C. L., Korth, H., Winslow, R. M., Borovsky, J. E., Purucker, M. E., ... McNutt, R. L., Jr. (2012, December). Low-degree structure in Mercury's planetary magnetic field. *Journal of Geophysical Research (Planets)*, *117*, E00L12. doi: 10.1029/2012JE004159

Aubert, J. (2013, February). Flow throughout the Earth's core inverted from geomagnetic observations and numerical dynamo models. *Geophys. J. Int.*, *192*(2), 537-556. doi: 10.1093/gji/ggs051

Bloxham, J., & Gubbins, D. (1987). Thermal core-mantle interactions. *Nature*, *325*, 511-513.

Bloxham, J., Gubbins, D., & Jackson, A. (1989). Geomagnetic secular variation. *Philos. Trans. R. Soc. London A*, *329*, 415-502.

Busse, F. H. (1975, January). A model of the geodynamo. *Geophys. J. Int.*, *42*, 437-459. doi: 10.1111/j.1365-246X.1975.tb05871.x

Cao, H., Aurnou, J. M., Wicht, J., Dietrich, W., Soderlund, K. M., & Russell, C. T. (2014, June). A dynamo explanation for Mercury's anomalous magnetic field. *Geophys. Res. Lett.*, *41*(12), 4127-4134. doi: 10.1002/2014GL060196

Christensen, U. (2006, December). A deep dynamo generating Mercury's magnetic field. *Nature*, *444*, 1056-1058. doi: 10.1038/nature05342

Christensen, U., Olson, P., & Glatzmaier, G. A. (1998, January). A dynamo model interpretation of geomagnetic field structures. *Geophys. Res. Lett.*, *25*(10), 1565-1568. doi: 10.1029/98GL00911

Christensen, U., & Wicht, J. (2008, July). Models of magnetic field generation in partly stable planetary cores: Applications to Mercury and Saturn. *Icarus*, *196*, 16-34. doi: 10.1016/j.icarus.2008.02.013

Christensen, U. R. (2018, 08). Geodynamo models with a stable layer and heterogeneous heat flow at the top of the core. *Geophysical Journal International*, *215*(2), 1338-1351. doi: 10.1093/gji/ggy352

Connerney, J. E. P., & Ness, N. F. (1988). Mercury's magnetic field and interior. In F. Vilas, C. R. Chapman, & M. S. Matthews (Eds.), *Mercury, university of arizona press* (p. 494-513).

Dumberry, M., & Rivoldini, A. (2015, Mar). Mercury's inner core size and core-crystallization regime. *Icarus*, *248*, 254-268. doi: 10.1016/j.icarus.2014.10.038

Finlay, C. C., Olsen, N., Kotsiaros, S., Gillet, N., & Tøffner-Clausen, L. (2016,

July). Recent geomagnetic secular variation from Swarm and ground observatories as estimated in the CHAOS-6 geomagnetic field model. *Earth, Planets, and Space*, *68*, 112. doi: 10.1186/s40623-016-0486-1

Genova, A., Goossens, S., Mazarico, E., Lemoine, F. G., Neumann, G. A., Kuang, W., . . . Zuber, M. T.   (2019, Apr).   Geodetic Evidence That Mercury Has A Solid Inner Core.   *Geophys. Res. Lett.*, *46*(7), 3625-3633.   doi: 10.1029/2018GL081135

Gubbins, D.   (1975).   Can the Earth's magnetic field be sustained by core oscillations? *Geophys. Res. Lett.*, *2*, 409–412.

Gubbins, D. (1983). Geomagnetic field analysis – I. Stochastic inversion. *Geophys. J. R. astr. Soc.*, *73*, 641-652.

Gubbins, D., & Bloxham, J. (1987). Morphology of the geomagnetic field and implications for the geodynamo. *Nature*, *325*, 509-511.

Hauck, S. A., Margot, J.-L., Solomon, S. C., Phillips, R. J., Johnson, C. L., Lemoine, F. G., . . . Zuber, M. T.   (2013, Jun).   The curious case of Mercury's internal structure.   *Journal of Geophysical Research (Planets)*, *118*(6), 1204-1220. doi: 10.1002/jgre.20091

Holme, R., & Bloxham, J.   (1996).   The magnetic fields of Uranus and Neptune: Methods and models. *J. geophys. Res.*, *101*, 2177-2200.

Jackson, A., Jonkers, A. R. T., & Walker, M. R.   (2000).   Four centuries of geomagnetic secular variation from historical records.   *Phil. Trans. R. Soc. Lond. A*, *358*, 957-990.

Jackson, D. D. (1979). The use of a priori data to resolve nonuniqueness in linear inversion. *Geophys. J. R. astr. Soc.*, *57*, 137-157.

Jault, D.   (2008).   Axial invariance of rapidly varying diffusionless motions in the Earth's core interior.   *Phys. Earth Planet. Inter.*, *166*, 67-76.   doi: 10.1016/j.pepi.2007.11.001

Johnson, C. L., Purucker, M. E., Korth, H., Anderson, B. J., Winslow, R. M., Al Asad, M. M. H., . . . Solomon, S. C.   (2012, December).   MESSENGER observations of Mercury's magnetic field structure.   *Journal of Geophysical Research (Planets)*, *117*, E00L14. doi: 10.1029/2012JE004217

Lesur, V., Wardinski, I., Rother, M., & Mandea, M.   (2008).   GRIMM - The GFZ Reference Internal Magnetic Model based on vector satellite and observatory

616   data. *Geophys. J. Int.*, *173*, 382-394. doi: 10.1111/j.1365-246X.2008.03724.x

617 Long, R. S., Mound, J. E., Davies, C. J., & Tobias, S. M. (2020, April). Scaling be-

618   haviour in spherical shell rotating convection with fixed-flux thermal boundary

619   conditions. *Journal of Fluid Mechanics*, *889*, A7. doi: 10.1017/jfm.2020.67

620 Lowes, F. J. (1966). Mean-square values on sphere of spherical harmonic vector

621   fields. *J. geophys. Res.*, *71*, 2179.

622 Manglik, A., Wicht, J., & Christensen, U. R. (2010, January). A dynamo model

623   with double diffusive convection for Mercury's core. *Earth and Planetary Sci-*

624   *ence Letters*, *289*(3-4), 619-628. doi: 10.1016/j.epsl.2009.12.007

625 Margot, J.-L., Hauck, I., Steven A., Mazarico, E., Padovan, S., & Peale, S. J. (2018,

626   June). Mercury's Internal Structure. *arXiv e-prints*, arXiv:1806.02024.

627 Mauersberger, P. (1956). Das Mittel der Energiedichte des geomagnetischen Haupt-

628   feldes an der Erdoberfläche und seine säkulare Änderung. *Gerlands Beiträge*

629   *zur Geophysik*, *65*, 207-215.

630 Ness, N. F. (1979, November). The magnetic field of Mercury. *Phys. Earth Planet.*

631   *Inter.*, *20*, 209-217. doi: 10.1016/0031-9201(79)90044-X

632 Ness, N. F., Behannon, K. W., Lepping, R. P., Whang, Y. C., & Schatten, K. H.

633   (1974, July). Magnetic Field Observations near Mercury: Preliminary Results

634   from Mariner 10. *Science*, *185*, 151-160. doi: 10.1126/science.185.4146.151

635 Oliveira, J. S., Hood, L. L., & Langlais, B. (2019, Sep). Constraining the Early

636   History of Mercury and Its Core Dynamo by Studying the Crustal Magnetic

637   Field. *Journal of Geophysical Research (Planets)*, *124*(9), 2382-2396. doi:

638   10.1029/2019JE005938

639 Oliveira, J. S., Langlais, B., Pais, M. A., & Amit, H. (2015, June). A modified

640   Equivalent Source Dipole method to model partially distributed magnetic field

641   measurements, with application to Mercury. *Journal of Geophysical Research*

642   *(Planets)*, *120*, 1075-1094. doi: 10.1002/2014JE004734

643 Olsen, N., Lühr, H., Sabaka, T. J., Mandea, M., Rother, M., Tøffner-Clausen, L., &

644   Choi, S. (2006). CHAOS-a model of the Earth's magnetic field derived from

645   CHAMP, Ørsted, and SAC-C magnetic satellite data. *Geophysical Journal*

646   *International*, *166*, 67-75. doi: 10.1111/j.1365-246X.2006.02959.x

647 Olson, P., Christensen, U., & Glatzmaier, G. A. (1999). Numerical modeling of

648   the geodynamo: Mechanisms of field generation and equilibration. *J. geophys.*

Res., *104*, 10383-10404. doi: 10.1029/1999JB900013

Olson, P., Landeau, M., & Reynolds, E.   (2018, Oct).   Outer core stratification from the high latitude structure of the geomagnetic field.   *Frontiers in Earth Science*, *6*, 140. doi: 10.3389/feart.2018.00140

Panovska, S., Korte, M., & Constable, C. G.   (2019, Dec).   One Hundred Thousand Years of Geomagnetic Field Evolution.   *Reviews of Geophysics*, *57*(4), 1289-1337. doi: 10.1029/2019RG000656

Peña, D., Amit, H., & Pinheiro, K. J. (2016, May). Magnetic field stretching at the top of the shell of numerical dynamos.   *Earth, Planets, and Space*, *68*(1), 78. doi: 10.1186/s40623-016-0453-x

Peale, S. J., Margot, J.-L., Hauck, S. A., & Solomon, S. C.   (2016, Jan).   Consequences of a solid inner core on Mercury's spin configuration. *Icarus*, *264*, 443-455. doi: 10.1016/j.icarus.2015.09.024

Shure, L., Parker, R. L., & Backus, G. E. (1982). Harmonic splines for geomagnetic modelling. *Phys. Earth Planet. Inter.*, *28*, 215-229.

Smith, D. E., Zuber, M. T., Phillips, R. J., Solomon, S. C., Hauck, S. A., Lemoine, F. G., . . . Taylor, A. H.   (2012, Apr).   Gravity Field and Internal Structure of Mercury from MESSENGER.   *Science*, *336*(6078), 214.   doi: 10.1126/science.1218809

Stanley, S. (2010, March). A dynamo model for axisymmetrizing Saturn's magnetic field. *Geophys. Res. Lett.*, *37*(5), L05201. doi: 10.1029/2009GL041752

Stanley, S., Bloxham, J., Hutchison, W. E., & Zuber, M. T. (2005, May). Thin shell dynamo models consistent with Mercury's weak observed magnetic field. *Earth and Planetary Science Letters*, *234*, 27-38. doi: 10.1016/j.epsl.2005.02.040

Stanley, S., & Mohammadi, A.   (2008, Jul).   Effects of an outer thin stably stratified layer on planetary dynamos. *Phys. Earth Planet. Inter.*, *168*(3-4), 179-190. doi: 10.1016/j.pepi.2008.06.016

Stevenson, D. J.   (1982, January).   Reducing the non-axisymmetry of a planetary dynamo and an application to saturn.   *Geophys. Astrophys. Fluid Dyn.*, *21*(1), 113-127. doi: 10.1080/03091928208209008

Takahashi, F., Shimizu, H., & Tsunakawa, H. (2019, January). Mercury's anomalous magnetic field caused by a symmetry-breaking self-regulating dynamo.   *Nature Communications*, *10*, 208. doi: 10.1038/s41467-018-08213-7

Tarantola, A. (1987). *Inverse problem theory. Methods for data fitting and model parameter estimation.* Amsterdam: Elsevier, 1987.

Thébault, E., Finlay, C. C., Alken, P., Beggan, C. D., Canet, E., Chulliat, A., ... Schachtschneider, R. (2015, July). Evaluation of candidate geomagnetic field models for IGRF-12. *Earth, Planets, and Space*, *67*, 112. doi: 10.1186/s40623-015-0273-4

Thébault, E., Finlay, C. C., Beggan, C. D., Alken, P., Aubert, J., Barrois, O., ... Zvereva, T. (2015). International Geomagnetic Reference Field: the 12th generation. *Earth, Planets, and Space*, *67*, 79. doi: 10.1186/s40623-015-0228-9

Thébault, E., Langlais, B., Oliveira, J. S., Amit, H., & Leclercq, L. (2018, March). A time-averaged regional model of the Hermean magnetic field. *Phys. Earth Planet. Inter.*, *276*, 93-105. doi: 10.1016/j.pepi.2017.07.001

Tian, Z., Zuber, M. T., & Stanley, S. (2015, November). Magnetic field modeling for Mercury using dynamo models with a stable layer and laterally variable heat flux. *Icarus*, *260*, 263-268. doi: 10.1016/j.icarus.2015.07.019

Uno, H., Johnson, C. L., Anderson, B. J., Korth, H., & Solomon, S. C. (2009, August). Modeling Mercury's internal magnetic field with smooth inversions. *Earth and Planetary Science Letters*, *285*, 328-339. doi: 10.1016/j.epsl.2009.02.032

Van Hoolst, T., Rivoldini, A., Baland, R.-M., & Yseboodt, M. (2012, Jun). The effect of tides and an inner core on the forced longitudinal libration of Mercury. *Earth and Planetary Science Letters*, *333*, 83-90. doi: 10.1016/j.epsl.2012.04.014

Vilim, R., Stanley, S., & Hauck, S. A. (2010, November). Iron snow zones as a mechanism for generating Mercury's weak observed magnetic field. *Journal of Geophysical Research (Planets)*, *115*(E11), E11003. doi: 10.1029/2009JE003528

Wardinski, I., Langlais, B., & Thbault, E. (2019). Correlated time-varying magnetic fields and the core size of mercury. *Journal of Geophysical Research: Planets*, *124*(8), 2178-2197. doi: 10.1029/2018JE005835

Wessel, P., Smith, W. H. F., Scharroo, R., Luis, J., & Wobbe, F. (2013). Generic mapping tools: Improved version released. *Eos, Transactions American Geophysical Union*, *94*(45), 409-410. doi: https://doi.org/10.1002/2013EO450001

Winslow, R. M., Anderson, B. J., Johnson, C. L., Slavin, J. A., Korth, H., Purucker,

M. E., ... Solomon, S. C. (2013). Mercury's magnetopause and bow shock from MESSENGER Magnetometer observations. *J. Geophys. Res., 118*. doi: 10.1002/jgra.50237
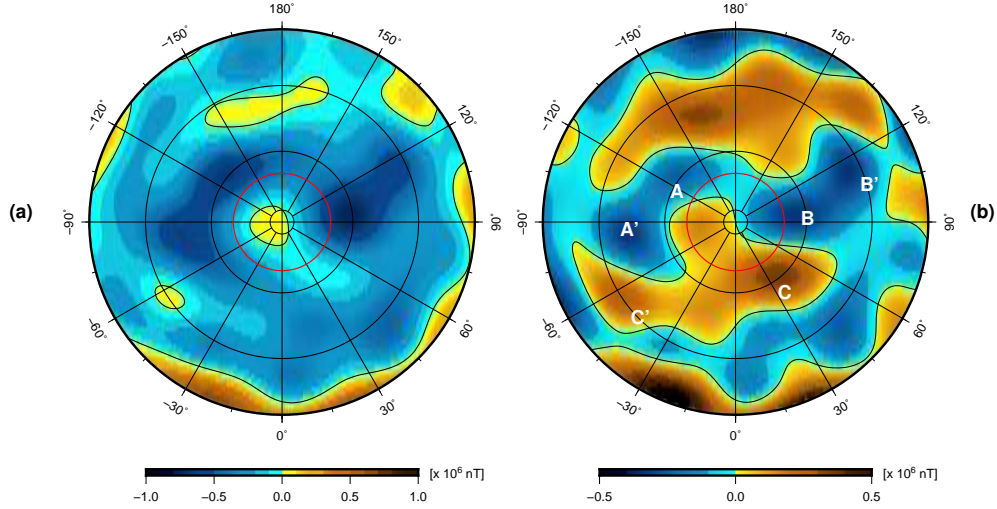
Figure A.1. North polar views of the radial magnetic field component (a) and its non-axisymetric part (b) at Earth's core surface. The red circles represent the diameter of Earth's inner core.

A   Earth's core field

Figure A.1 shows the radial geomagnetic field component and its non-axisymmetric part at Earth's core surface in the year 2015. The maps are based on the 12[th]International geomagnetic reference field (Thébault, Finlay, Beggan, et al., 2015). The model was truncated at spherical harmonic degree $L_{\mathrm{int}} = 10$. The maps show also the projection of the inner core tangent cylinder on the CMB.

B   Covariance analysis

We study the robustness of our inversion results by analyzing the resolution matrix. Yet, another way to estimate formal uncertainties of the results is by analyzing the covariance matrix, which is given by

$$\mathbf{C} = \hat{\sigma}^2 (\mathbf{A}^\mathsf{T} \mathbf{C_e}^{-1} \mathbf{A} + \lambda_s \mathbf{C_m}^{-1})^{-1}, \tag{B.1}$$

where $\hat{\sigma}^2$ is the misfit between model and data. These errors are formal, as they represent the uncertainty in the model subject with respect to the constraint and may be invalidated by false observations or by inappropriate prior information. It does not contain that part of the uncertainty, which is related to a trade-off in resolution, when combinations of parameters have the same effect on the fit to the data (Bloxham et al., 1989).
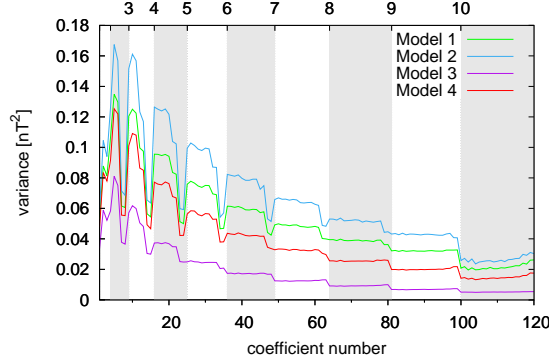
Figure B.1. Diagonal terms of the four models covariance matrices.

In this sense, diagonal elements of **C** are the formal variances of the model parameters, and the off-diagonal elements are the formal covariance between individual model parameters.

In Figure B.1 the diagonal elements of the four models covariance matrices are shown. The largest variances are found for coefficients of spherical harmonic degrees 2 and 3, i.e. g_2^1 and g_3^1. Generally, the formal error is small, and depends on the strength of the damping parameter λ_s; weaker damping enhances the formal error.

Figure B.2 shows the scaled covariance matrix elements of the four models. These matrix elements are scaled by the variances of the diagonal elements. This scaling procedure enhances covariance structures of the non-diagonal elements. The scaled covariance matrices of Models 1, 2, and 4 are very similar in their off-diagonal structures, whereas those structures are rather faint in the covariance matrix of Model 3. Large negative covariance (blue) occur between g_2^0 and coefficients of the first spherical harmonic degree (lower left corner of each plot). This trend continues between coefficients of consecutive spherical harmonic degrees e.g. $C(g_3^1, g_4^1)$, which leads to 'parallel' off-diagonal structures. Positive covariance structures are less pronounced and occur between coefficients with two spherical harmonic degrees differences e.g. $C(g_2^0, g_4^0)$. These structures are mostly visible for Models 1 and 2. The cause of these off-diagonal structures is the uneven hemispherical data distribution.
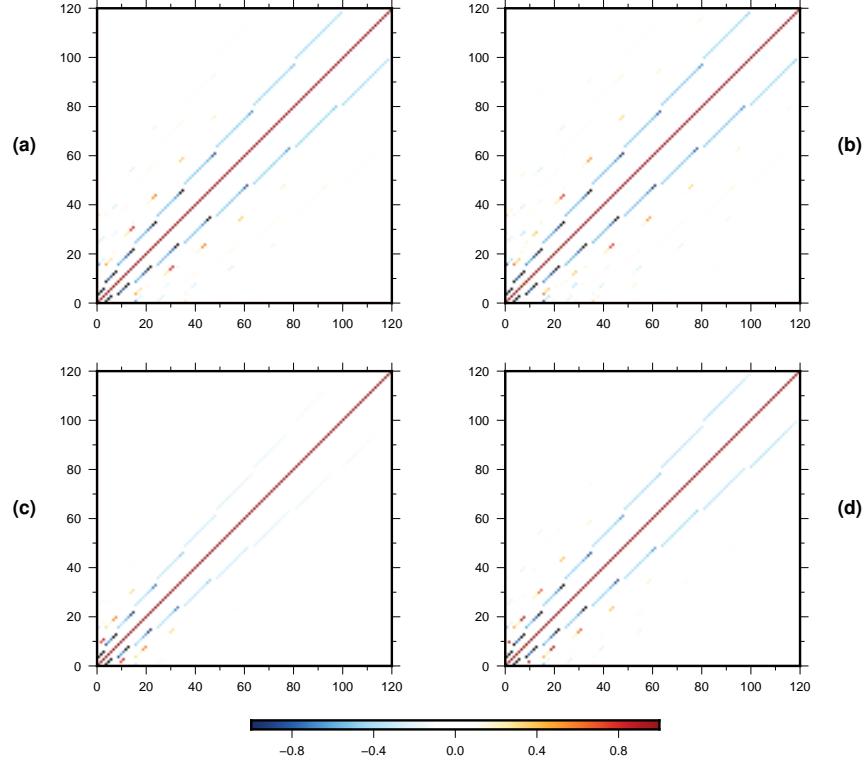
Figure B.2. Covariance matrix elements of the four model solutions. Elements are scaled by the covariance of the diagonal elements $C(g_n^n, g_n^n)$ to enhance the visibility of the non-diagonal terms. a, b, c and d refer to matrices of Models 1, 2, 3 and 4, respectively.